RSC Advances

PAPER

View Article Online
View Journal | View Issue

Cite this: *RSC Adv.*, 2021, **11**, 13731

Few-layer $Bi_2O_2CO_3$ nanosheets derived from electrochemically exfoliated bismuthene for the enhanced photocatalytic degradation of ciprofloxacin antibiotic

Hangdao Qin, [ab] Yingchang Yang, *[a] Wei Shi[a] and Yuanbin She [b]

Received 21st January 2021
Accepted 5th March 2021

DOI: 10.1039/d1ra00528f

rsc.li/rsc-advances

Few-layer two-dimensional (2D) $Bi_2O_2CO_3$ nanosheets with a thickness of 4–5 nm were successfully fabricated *via* electrochemical exfoliation, followed by an exposure to ambient conditions. The formation process for these nanosheets was explored through *ex situ* X-ray diffractometer. The photocatalytic capacity of 2D $Bi_2O_2CO_3$ nanosheets was investigated towards the degradation of ciprofloxacin. It was shown that 2D $Bi_2O_2CO_3$ nanosheets exhibited better catalytic performance than $Bi_2O_2CO_3$ nanoparticles synthesized by hydrothermal method under UV-Vis light irradiation. The enhanced photocatalytic activity is due to the larger specific surface area, as well as the lower band gap. Additionally, the radical trap experiments demonstrate that holes and hydroxyl radicals are of great importance in the degradation of ciprofloxacin. Finally, the 2D $Bi_2O_2CO_3$ nanosheets show high stability in the photocatalytic degradation of ciprofloxacin, and could have a prospective application in the treatment of antibiotic wastewater.

1. Introduction

The removal of antibiotics from wastewater is significant since many antibiotics are refractory to biodegradation, and they will lead to the emergence of another global environmental pollution problem.[1] Ciprofloxacin, as the second generation fluoroquinolone antibiotics, has been widely used in human treatment and animal husbandry.[2] The release of ciprofloxacin into wastewater and its accumulation in the aquatic environment will bring the potential risk to aquatic ecosystems and human health.[3] The development of new technologies for the degradation of such antibiotics into CO_2, H_2O, and other non-toxic small molecules is a great concern.

Photocatalysis technology has proven to be an effective technology for the degradation of refractory organic compounds due to the highly reactive species generated in the interaction of the photocatalyst and UV light.[4,5] The most widely used photocatalysts are TiO_2 nanoparticles.[6,7] However, due to their lower activity under visible light, many attempts have been made to look for alternatives. Recently, Bi-containing complex oxides have been found to be very effective in the degradation of organic contaminants under visible light irradiation.[8,9] Among these oxides, $Bi_2O_2CO_3$ has been studied by many researchers due to its layered structure, the ease of synthetic methods, the availability of precursors and nontoxic nature.[10,11] Doping and coupling with other oxides can enhance the photocatalysis properties and efficiency of $Bi_2O_2CO_3$.[12,13] However, they will complicate the synthetics severely and increase the cost. Moreover, controlling the morphology of nanostructured $Bi_2O_2CO_3$ seems to be a feasible way to improve the photocatalysis efficiency, as the morphology of nanomaterials has an impact on their catalytic performance. $Bi_2O_2CO_3$ with different morphologies can be synthesized traditionally *via* solvothermal method by controlling the precursors, reactant ratios, and reaction temperature.[14] However, to obtain ultrathin two-dimensional (2D) $Bi_2O_2CO_3$ nanosheets with excellent photocatalytic activity is still a challenge. In 2013, Ag-doped $Bi_2O_2CO_3$ microspheres comprising nanoplates (12 nm in thickness) were successfully fabricated through a hydrothermal method, and it showed improved photocatalytic activity towards methyl orange (MO) dye.[15] Nevertheless, the synthesis process requires the addition of a polyvinylpyrrolidone template and KCl salt, and the loading of Ag nanoparticles. More recently, few-layer $Bi_2O_2CO_3$ was fabricated through the electrochemical exfoliation of bulk Bi in 0.5 M Na_2CO_3 solution.[16] This few-layer $Bi_2O_2CO_3$ with a thickness of six atomic layers exhibits good activity and selectivity towards CO_2 electro-reduction. In their results, $Bi_2O_2CO_3$ was constructed through the reaction of oxidised exfoliated bismuth nanosheets with CO_3^{2-} in the electrolyte. This method is facile and requires no surfactant. However, the Na^+ intercalating agent used here is too small to

[a]College of Material and Chemical Engineering, Tongren University, Tongren 554300, China. E-mail: yangyc612@gmail.com

[b]College of Chemical Engineering, Zhejiang University of Technology, Hangzhou 310014, China

exfoliate bismuth effectively, which will greatly reduce the synthesis efficiency.

In the current work, two-dimensional (2D) bismuthene nanosheets were fabricated through the electrochemical cathodic exfoliation of bulk Bi in a *N*,*N*-dimethylformamide solution of quaternary ammonium salt. These nanosheets were very unstable, even in ambient condition, as their ultrathin structures. When exposed to room air for a few days, they can be gradually transformed into ultrathin 2D $Bi_2O_2CO_3$ nanosheets (4–5 nm in thickness) spontaneously. As a contrast, $Bi_2O_2CO_3$ nanoparticles were synthesized by a traditionally hydrothermal method. The photocatalytic performances of these nanomaterials were evaluated in the photocatalytic degradation of ciprofloxacin in aqueous solution. To study the effect of the main active species in the degradation of ciprofloxacin, different scavengers were used to investigate the contribution of several active species. Furthermore, the stability of the as-prepared photocatalysts was evaluated.

2. Experimental

2.1. Reagents and materials

The commercial ciprofloxacin (PKU Healthcare Corp., Ltd.) was used without further purification. Lithium hexafluorophosphate ($LiPF_6$, 98%), sodium hexafluorophosphate ($NaPF_6$, 98%), tetramethylammonium hexafluorophosphate (TMAP, 99%), tetraethylammonium hexafluorophosphate (TEAP, 99%), tetrabutylammonium hexafluorophosphate (TBAP, 99%), tetraheptylammonium bromide (THAB, 99%), and *N*,*N*-dimethylformamide (DMF, 99.9%) were purchased from Alfa Aesar. Bismuth(III) nitrate pentahydrate ($(BiNO_3)_3 \cdot 5H_2O$), urea and anhydrous ethanol were obtained from Shanghai Sinopharm Chemical Reagent Co., Ltd. Titanium dioxide (TiO_2, P25) was purchased from Shanghai Yien Chemical Technology Co., Ltd. Triethanolamine (TEA), *p*-benzoquinone (BQ) and *tert*-butylalcohol (*t*-BuOH) were purchased from Shanghai Macklin Biochemical Co., Ltd. All chemicals were at reagent or above purity, and were used without further purification. Deionized water was used throughout the experiments.

2.2. Preparation of $Bi_2O_2CO_3$

First, 2D bismuthene nanosheets were fabricated through electrochemically cathodic exfoliation of bulk Bi rod. The bulk bismuth rod (99.999%, 5 mm in diameter, 2 cm in length) and the platinum sheet (20 mm in length, 20 mm in width) were adopted as the cathode and anode, respectively. 0.5 M TEAP in DMF solution (50 mL) was utilized as the electrolyte. A direct current voltage of 6 V was applied for the exfoliation to proceed for 2 h. The black exfoliated bismuthene product was washed thoroughly with DMF and ethanol for six times, and dried in a vacuum oven at 60 °C. Then, the exfoliated 2D bismuthene was transformed into 2D $Bi_2O_2CO_3$ (labelled as E-$Bi_2O_2CO_3$) naturally when it was exposed to room temperature (25 °C). For comparison, $Bi_2O_2CO_3$ nanoparticles (labelled as H-$Bi_2O_2CO_3$) were obtained by a traditionally hydrothermal method.[11]

2.3. Characterization

The X-ray diffraction patterns of the samples were carried out on the Bruker X-ray diffractometer (XRD, D8 Advance) using Cu Kα. An Autosorb-iQA3200-4 sorption analyzer (Quantatech Co., USA) based on N_2 adsorption/desorption was used to measure the Brunauer–Emmett–Teller specific (BET) surface area. The surface morphology and thickness of the $Bi_2O_2CO_3$ samples were examined with a field emission scanning electron microscope (FESEM, Hitachi S4800), transmission electron microscope (TEM, JEM-2100F), and atomic force microscope (AFM, Dimension V, Veeco). The surface chemical valences of the $Bi_2O_2CO_3$ catalyst were analysed with an ESCALAB 250 X-ray photoelectron spectroscope (XPS). The UV-visible diffuse reflectance spectra were measured with a Hitachi UV-3310. The photoluminescence (PL) spectra were collected on a Hitachi F4600 fluorescence spectrophotometer, using a Xe lamp (excitation at 365 nm) as the light source.

2.4. Photocatalytic experiments

A homemade photocatalytic reactor equipped with a water-cooling device and a 300 W xenon lamp was utilized to detect the photocatalytic degradation of ciprofloxacin antibiotic. 10 mg L^{-1} ciprofloxacin solution (150 mL) was placed in the reactor, and then 150 mg of photocatalyst was added and stirred magnetically in the dark for 0.5 h to establish the adsorption equilibrium. The residual of ciprofloxacin after photocatalytic degradation for a certain time was taken out with a syringe, and centrifuged immediately for further concentration measurement with a high performance liquid chromatograph (Shimadzu Prominence LC-20AT, UV detector, C18 reverse phase column, 4.6 × 250 mm, 5 μm) under a wavelength of 278 nm. The mobile phase was an acetonitrile-ultrapure water (1 : 4, v/v) mixed solution, and the flow rate was 0.8 mL min^{-1}. The initial pH was adjusted by adding 0.1 mol L^{-1} HCl or 0.1 mol L^{-1} NaOH solution. The total organic carbon (TOC) was measured using a Shimadzu TOC-5000A analyser. The toxicity of ciprofloxacin and its degradation products was examined by plate count method using *Escherichia coli* as the reference microorganism.[17]

3. Results and discussion

3.1. Preparation mechanism exploration

The stable form of bulk bismuth crystal in nature comprises parallel buckled rhombohedral layers (space group $R\bar{3}m$).[18] With a layered structure (Scheme 1), it provides a possibility for the intercalation of cations/anions and solvents, expansion, and exfoliation into few layers under the driven force. Herein, an electrochemical exfoliation strategy (shown in Scheme 1) was developed to peel off bulk bismuth into 2D bismuthene nanosheets in the DMF solution of $(CH_3CH_2)_4N^+PF_6^-$ (TEAP). In pursuit of an ideal inserting cation, various ions with different sizes, including Li^+, Na^+, tetramethylammonium cation (TMA^+), tetraethylammonium cation (TEA^+), tetrabutylammonium cation (TBA^+), and tetraheptylammonium cation (THA^+) were examined. Alkali ions, such as Li^+ or Na^+, were expected to

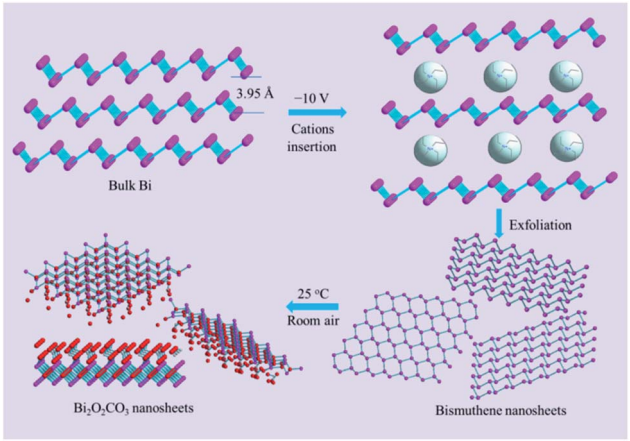

Scheme 1 Scheme illustration for the synthesis of 2D $Bi_2O_2CO_3$ nanosheets through electrochemical exfoliation, followed by exposure to ambient condition.

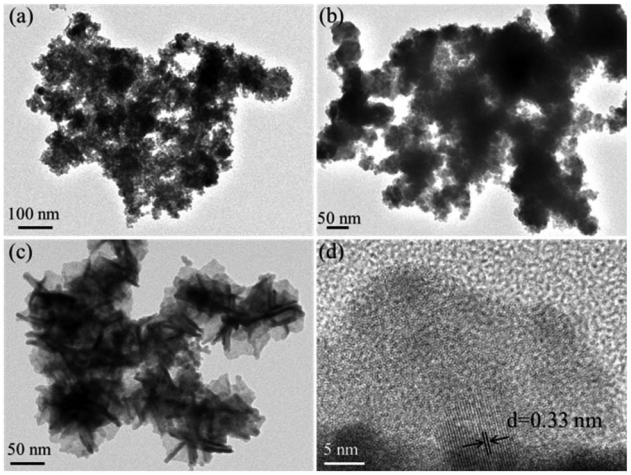

Fig. 1 TEM images of the Bi product exfoliated in the electrolyte of TBA^+ (a), THA^+ (b), and TEA^+ (c), and HRTEM image (d) of the exfoliated Bi product in the electrolyte of TEA^+.

intercalate into bulk bismuth. However, they are too small (Li^+ 0.9 Å in radius; Na^+ 1.2 Å),[19,20] and only intermetallic compounds (for example, Li_3Bi and Na_3Bi) would be formed when a negative potential of −6 V was applied for 2 h. These intermetallic compounds are stable in an inert environment, but they can be easily oxidized by proton solvents (*e.g.*, H_2O and C_2H_5OH). Therefore, the surface of bulk bismuth after being polarized for 2 h could be dispersed into tiny amounts of black Bi sols when placed into H_2O or C_2H_5OH. In comparison with alkali ions such as Li^+ and Na^+, tetraalkylammonium cations usually display larger diameters (*e.g.*, TMA^+ 5.6 Å, TEA^+ 6.7 Å, TBA^+ 8.3 Å, and tetraheptylammonium bromide (THAB; $d \approx 20$ Å)), and they are larger than the interlamellar space of bulk bismuth (3.95 Å).[19,21] It is noted that only a thin layer of spongy black substance was generated on the surface of the bulk bismuth electrode when it was exfoliated in the electrolyte of TMA^+ even under a highly negative potential of −10 V for 6 h, indicating that the TMA^+ cations were not big enough to delaminate the bulk bismuth. Nevertheless, when a moderate voltage of −6 V was applied, the rapid delamination of bulk bismuth into dark sol, together with small amounts of bubbles, were observed within seconds in the electrolyte of TEA^+, TBA^+, or THA^+. After exfoliation for 6 h, the dark sols were washed and further characterized.

The TEM images of the exfoliated Bi products in TBA^+, THA^+, and TEA^+ solutions are shown in Fig. 1a–c, respectively. It is clear that both of the exfoliated Bi products in the electrolytes of TBA^+ and THA^+ display the features of Bi nanoparticles. Fig. 1c and d exhibit the typical TEM and HRTEM images of the exfoliated materials in the electrolyte of TEA^+. The TEM image (Fig. 1a) shows that this exfoliated Bi product comprises ultrathin nanosheets. As can be seen in the HRTEM image (Fig. 1b), obvious lattice fringes with a space of 0.33 nm can be observed, which correspond to the (012) plane of the layered Bi crystal, confirming the formation of the 2D bismuthene nanosheets. These results clearly reveal that the TEA^+ cation with a diameter of 6.7 Å is the best intercalating agent for the exfoliation of 2D bismuthene nanosheets. Interestingly, the as-exfoliated ultrathin 2D bismuthene nanosheets in the electrolyte of TEA^+ are prone to oxidation even exposed to room air (Scheme 1), which provides a facile and feasible way for the synthesis of 2D $Bi_2O_2CO_3$ at room temperature. It was found that the bismuthene nanosheets obtained in the electrolyte of TEA^+ could be completely transformed into greyish white $Bi_2O_2CO_3$ when exposed to room air for seven days, while it would take twenty days and a month for products to be exfoliated in the electrolyte of TBA^+ and THA^+, respectively.

Fig. 2a displays the XRD patterns of the as-exfoliated 2D bismuthene nanosheets and the samples that were exposed to room air for one day to seven days. The diffraction peaks for the as-exfoliated 2D bismuthene nanosheets at 22.3°, 27.1°, 37.8°, 39.5°, 48.7°, 55.9°, 64.5°, and 70.7° can be indexed to the planes of β-Bi (003), (012), (104), (110), (202), (024), (122), and (214), respectively, according to the XRD standard card for β-Bi (JCPDS card no. 44-1246).[22] No diffraction peaks for other phases could be observed, illustrating that the pure material was obtained. When the 2D bismuthene sample was exposed to room air for one day to seven days, the typical characteristic diffraction

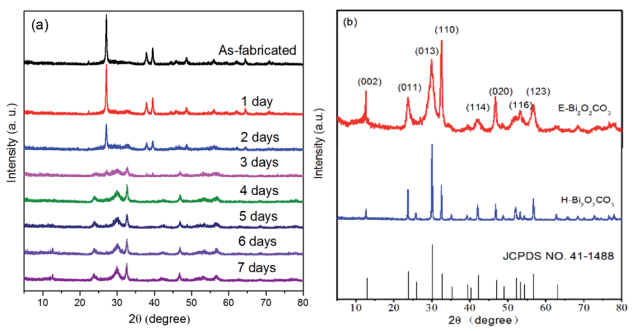

Fig. 2 (a) XRD patterns of the as-exfoliated 2D bismuthene nanosheets, and the samples that were exposed to room air for one day to seven days; (b) XRD patterns of E-$Bi_2O_2CO_3$ and H-$Bi_2O_2CO_3$.

peaks for bismuthene gradually disappeared, while the characteristic diffraction peaks for $Bi_2O_2CO_3$ (JCPDS card no. 41-1488) increased steadily.[11] Lastly, only the characteristic diffraction peaks for $Bi_2O_2CO_3$ can be observed, indicating that the as-exfoliated 2D bismuthene was completely converted to $Bi_2O_2CO_3$ after exposed to room air for seven days. It should be noted that increasing the temperature and air humidity could greatly reduce the reaction time.

3.2. Characterization of $Bi_2O_2CO_3$

XRD patterns of the as-prepared E-$Bi_2O_2CO_3$, H-$Bi_2O_2CO_3$, and the PDF standard card of the layered $Bi_2O_2CO_3$ are shown in Fig. 2b. The diffraction peaks for both samples can be clearly observed at 12.7°, 23.9°, 30.4°, 32.6°, 42.1°, 46.7°, 53.5° and 56.9°, which are consistent with the PDF standard card of tetragonal $Bi_2O_2CO_3$ (JCPDS card no. 41-1488).[11] Additionally, it can be found from Fig. 2b that the diffraction peaks of H-$Bi_2O_2CO_3$ are sharper and stronger than those of E-$Bi_2O_2CO_3$, indicating that the size of E-$Bi_2O_2CO_3$ is smaller than that of H-$Bi_2O_2CO_3$, according to Scherrer's equation. Fig. 3 exhibits the N_2 adsorption–desorption isotherms, and the corresponding pore size distribution curves of E-$Bi_2O_2CO_3$ and H-$Bi_2O_2CO_3$. As can be seen, both samples exhibit the representative isotherms of type IV and hysteresis loop type H3 at high relative pressure (P/P_0),[23] illustrating the presence of mesopores and slit-like pores formed by the aggregated sheet-like particles.[24,25] Moreover, it is seen that the area of the hysteresis loop for E-$Bi_2O_2CO_3$ is much larger than that of H-$Bi_2O_2CO_3$, indicating that the pore volume of E-$Bi_2O_2CO_3$ is much higher than that of H-$Bi_2O_2CO_3$, which can also been seen in the pore size distribution curves (Fig. 3b).

Table 1 exhibits the textural parameters of the BET surface area (S_{BET}) and pore volume for E-$Bi_2O_2CO_3$ and H-$Bi_2O_2CO_3$. It is clear that the S_{BET} and pore volume of E-$Bi_2O_2CO_3$ fabricated through electrochemical exfoliation followed by spontaneous oxidation here are much larger than those of H-$Bi_2O_2CO_3$ synthesized *via* hydrothermal method, suggesting the advantage of this electrochemical method, which will greatly improve the photocatalytic performance of the photocatalyst.[11] In comparison with the various structured $Bi_2O_2CO_3$ materials prepared through hydrothermal method, the specific surface area of the few-layer E-$Bi_2O_2CO_3$ nanosheets (97 $m^2\ g^{-1}$) here is much larger than that of the flower-like $Bi_2O_2CO_3$ (20.43 $m^2\ g^{-1}$), sponge-like $Bi_2O_2CO_3$ (50.60 $m^2\ g^{-1}$) and plate-like $Bi_2O_2CO_3$ (4.30 $m^2\ g^{-1}$).[26]

Table 1 The physical and chemical properties of E-$Bi_2O_2CO_3$ and H-$Bi_2O_2CO_3$

Samples	S_{BET} ($m^2\ g^{-1}$)	Pore volume ($cm^3\ g^{-1}$)	Thickness (nm)	Band gap (eV)
E-$Bi_2O_2CO_3$	97	0.49	4–5	2.95
H-$Bi_2O_2CO_3$	21	0.12	—	3.22

The SEM, TEM and AFM images of E-$Bi_2O_2CO_3$ and H-$Bi_2O_2CO_3$ are shown in Fig. 4. The SEM images in Fig. 4a and b indicate that E-$Bi_2O_2CO_3$ consisted of well-defined nanosheets, and particles with other morphologies cannot be observed. In contrast, H-$Bi_2O_2CO_3$ comprises irregular particles with different sizes. Moreover, it is seen from Fig. 4a and b that the size of E-$Bi_2O_2CO_3$ is smaller than that of H-$Bi_2O_2CO_3$, which is consistent with the result obtained by XRD. As shown in Fig. 4c–f, the morphology and microstructure of E-$Bi_2O_2CO_3$ were further elucidated by TEM and AFM. The TEM images in Fig. 4c and d confirm that E-$Bi_2O_2CO_3$ comprises ultrathin nanosheets. The HRTEM image (Fig. 4e) reveals a lattice spacing of 0.272 nm, agreeing well with the spacing of the (110) plane of the tetragonal $Bi_2O_2CO_3$ crystal.[27] In addition, the SAED pattern in the inset of Fig. 4e demonstrates an array of orderly diffraction spots indexed to the (110), ($\bar{1}$10) and (020)

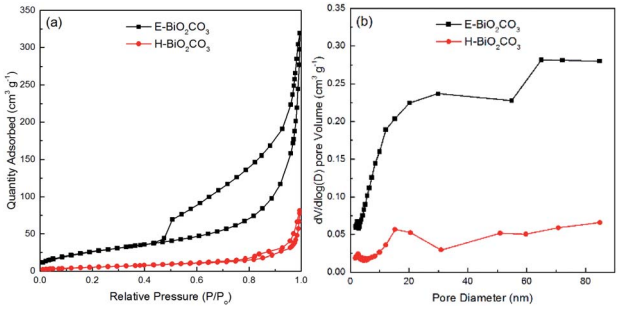

Fig. 3 N_2 adsorption–desorption isotherms (a), and the corresponding pore size distribution curves (b) of E-$Bi_2O_2CO_3$ and H-$Bi_2O_2CO_3$.

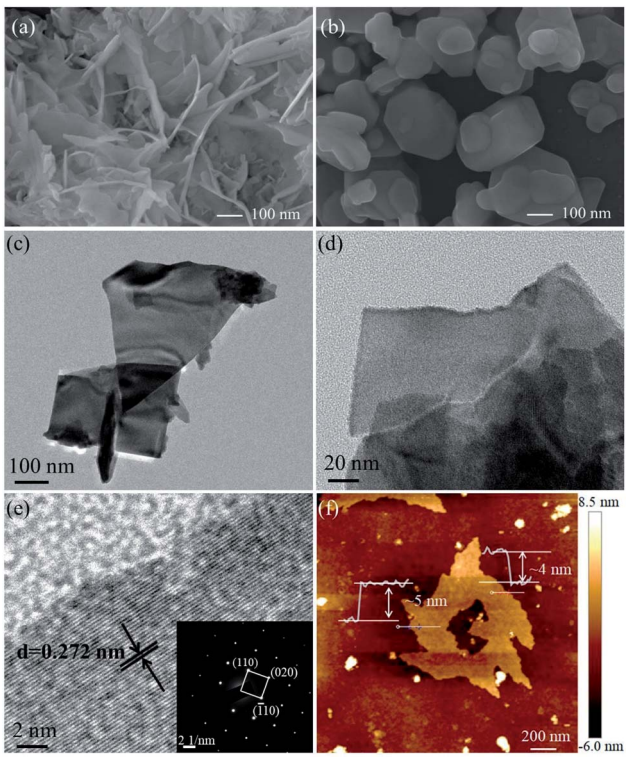

Fig. 4 SEM images of E-$Bi_2O_2CO_3$ (a) and H-$Bi_2O_2CO_3$ (b); TEM (c–e) and AFM (f) images of E-$Bi_2O_2CO_3$.

reflections, suggesting that the E-$Bi_2O_2CO_3$ nanosheet is a well-defined single-crystal.[27] Fig. 4f shows the AFM image of the E-$Bi_2O_2CO_3$ nanosheet. As can be seen, the topographical profiles in Fig. 4f demonstrate that the thickness of the E-$Bi_2O_2CO_3$ nanosheet is *ca.* 4.1–4.8 nm. According to the layer spacing of $Bi_2O_2CO_3$ (~0.68 nm), the layer number of E-$Bi_2O_2CO_3$ can be assigned to be 6–7 layers.

The surface composition and the chemical state of the as-fabricated few-layer E-$Bi_2O_2CO_3$ nanosheets were further investigated with XPS. The survey XPS spectrum of E-$Bi_2O_2CO_3$ shown in Fig. 5a suggests the presence of Bi, C and O elements. The semi-quantitative results indicate that the atomic percentage of C, O and Bi are 26.4%, 54.05% and 19.56%, respectively. The high-resolution spectra of Bi 4f, C 1s and O 1s are depicted in Fig. 5b–d, respectively. It can be clearly seen from Fig. 5b that there are two individual peaks at 164.7 eV and 159.4 eV, which can be ascribed to the binding energy of Bi $4f_{5/2}$ and Bi $4f_{7/2}$ states, respectively. The C 1s spectra display two clear peaks at 284.9 eV and 289.0 eV, which correspond to the adventitious hydrocarbon from the environment and the CO_3^{2-} in the E-$Bi_2O_2CO_3$ sample.[28] The O 1s spectra are shown in Fig. 5d, the well-defined peak centred at 530.7 eV can be ascribed to the carbonate species and adsorbed water on the $Bi_2O_2CO_3$ surface.[28]

As shown in Fig. 6a, the UV-Vis DRS of E-$Bi_2O_2CO_3$ and H-$Bi_2O_2CO_3$ nanomaterials were obtained through a UV-Vis spectrometer. It can be seen that the photoabsorption for both samples ranging from the UV light region to visible light are shorter than 450 nm. Additionally, steep absorption curves can be observed in both samples, exhibiting that the visible light absorption is ascribed to the band gap transition rather than the transition from the impurity level.[26] Furthermore, E-

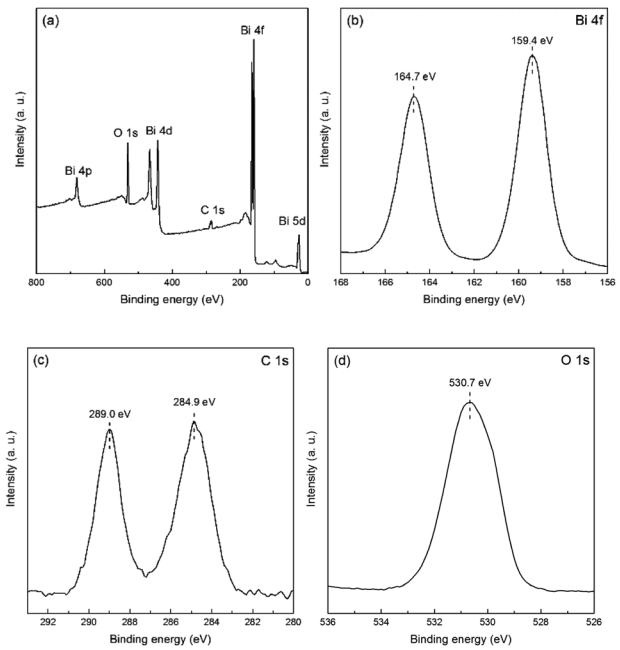

Fig. 5 XPS spectra of E-$Bi_2O_2CO_3$: survey (a), Bi 4f (b), C 1s (c) and O 1s (d).

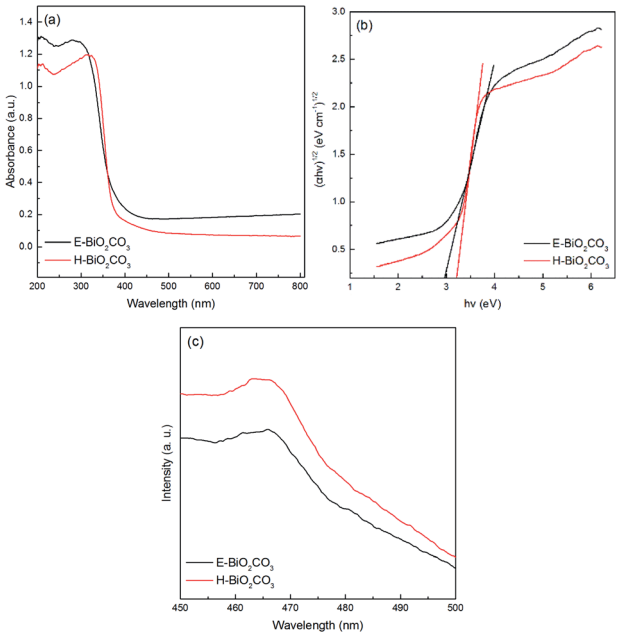

Fig. 6 UV-Vis DRS (a), plots of the energy of absorbed light (b) and PL spectra (c) of E-$Bi_2O_2CO_3$ and H-$Bi_2O_2CO_3$.

$Bi_2O_2CO_3$ shows an absorption edge at about 450 nm, while the absorption edge of H-$Bi_2O_2CO_3$ blue-shifted to 390 nm, which is due to the E-$Bi_2O_2CO_3$ fabricated through electrochemical exfoliation followed by spontaneous oxidation here is much thinner than that of H-$Bi_2O_2CO_3$ synthesized *via* hydrothermal method.[11] To measure the band gaps of the $Bi_2O_2CO_3$, the equation $\alpha h\nu = A(h\nu - E_g)^{n/2}$ is applied,[26] and the plot of $(\alpha h\nu)^{1/2}$ *vs.* energy $(h\nu)$ is displayed in Fig. 6b. It is clear that the band gaps estimated from the onset of the absorption edge are about 2.95 eV and 3.22 eV for E-$Bi_2O_2CO_3$ and H-$Bi_2O_2CO_3$, respectively. Moreover, it was found that the band gap of the as-fabricated E-$Bi_2O_2CO_3$ here is lower than that of the $Bi_2O_2CO_3$ nanomaterials synthesized through hydrothermal method or solvothermal method.[11,24,26] Furthermore, PL measurements can provide important information on the charge separation. As can be seen in Fig. 6c, the PL intensity of E-$Bi_2O_2CO_3$ is lower than that of H-$Bi_2O_2CO_3$, which implies that the ultrathin E-$Bi_2O_2CO_3$ can significantly restrain the recombination of the electron–hole pairs.

3.3. Photocatalytic degradation of ciprofloxacin

The photocatalytic performance of the $Bi_2O_2CO_3$ nanomaterials was estimated in the decomposition of ciprofloxacin under UV-Vis light irradiation. The experimental parameters were set at a ciprofloxacin concentration of 10 mg L^{-1}, pH value of 7.12, and catalyst dosage of 1.0 g L^{-1}. As presented in Fig. 7a, a negligible removal of ciprofloxacin was observed in the absence of catalyst, which indicated that single photolysis was insufficient to degrade this antibiotic. Besides, TiO_2 presented a limited catalytic activity in this study. However, E-$Bi_2O_2CO_3$ exhibited the highest adsorption and degradation efficiency towards ciprofloxacin. After stirring for 30 min in the dark,

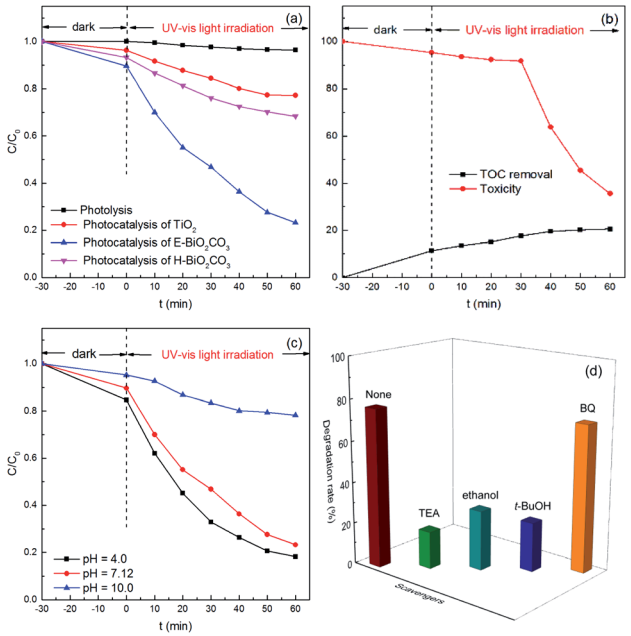

Fig. 7 (a) Photodegradation of ciprofloxacin in the presence of different photocatalysts; (b) the TOC and toxicity at different reaction times using the E-$Bi_2O_2CO_3$ photocatalyst under UV-Vis light irradiation; (c) effect of pH on the photodegradation of ciprofloxacin in the presence of E-$Bi_2O_2CO_3$ under UV-Vis light irradiation; (d) effects of radical scavengers on the ciprofloxacin degradation using the E-$Bi_2O_2CO_3$ photocatalyst under UV-Vis light irradiation.

10.4% of ciprofloxacin was removed by the E-$Bi_2O_2CO_3$ composite, which displayed enhanced adsorption capacity compared to H-$Bi_2O_2CO_3$. The improvement could be attributed to the superior surface area (Table 1). After irradiation for 60 min with UV-Vis light, E-$Bi_2O_2CO_3$ achieved 76.8% degradation of ciprofloxacin, which was remarkably high compared to that of H-$Bi_2O_2CO_3$ (31.7%) and TiO_2 (22.8%).

Compared to H-$Bi_2O_2CO_3$, E-$Bi_2O_2CO_3$ showed better catalytic performance. The enhanced catalytic activity of E-$Bi_2O_2CO_3$ may be ascribed to the following aspects. On the one hand, the specific surface area of E-$Bi_2O_2CO_3$ was much larger than that of H-$Bi_2O_2CO_3$ (Table 1). Ultrathin E-$Bi_2O_2CO_3$ nanosheets could increase the contact area between the catalyst and antibiotic molecules. The good adsorption capacity of E-$Bi_2O_2CO_3$ was also in favor of the reaction between the organics and active species on the surface of the catalyst.[11,29] On the other hand, the band gap determined the spontaneity of a photocatalytic reaction.[30,31] The band gap of E-$Bi_2O_2CO_3$ was less than that of H-$Bi_2O_2CO_3$ (Table 1), and therefore the photocatalysis over E-$Bi_2O_2CO_3$ was more reactive under UV-Vis light irradiation.

Mineralization of ciprofloxacin by E-$Bi_2O_2CO_3$ photocatalysis was estimated by measuring the TOC removal of the reaction solutions. As shown in Fig. 7b, although the removal rate of ciprofloxacin was nearly 76.8% (Fig. 7a), the TOC removal was only 20.5%. The results indicated that the aliphatic intermediates generated from the ring-opening reaction might be more resistant towards further mineralization. The toxicity at different reaction times was also presented in Fig. 7b, where the toxicity was almost unchanged in the first 30 min, and subsequently it was gradually decreased. At the end of 60 min treatment, the toxicity decreased to 35.5%, suggesting the effective elimination of the toxicity of ciprofloxacin and the intermediates by E-$Bi_2O_2CO_3$ photocatalysis.

The influence of the initial pH on ciprofloxacin degradation was investigated. It can be observed from Fig. 7c that the ciprofloxacin decay was strongly pH-dependent. E-$Bi_2O_2CO_3$ showed the highest photocatalytic activity at pH 4.0, while it presented the lowest photocatalytic performance at pH 10.0. These observations could be explained by the surface charge of ciprofloxacin, and E-$Bi_2O_2CO_3$ would be greatly affected by the solution pH.[17]

To identify the active species during the photocatalytic degradation of ciprofloxacin over E-$Bi_2O_2CO_3$, the trapping experiments were carried out by adding suitable radical scavengers. Undoubtedly, electrons (e^-) and holes (h^+) are the principal contributors to the generation of active species, and may therefore restrain the degradation of organic pollutants.[32,33] In the trapping experiments, TEA and anhydrous ethanol were used as the scavengers for holes and electrons, respectively. It can be seen from Fig. 7d that the removal efficiency of ciprofloxacin decreased from 76.8% to 18.0% in the presence of TEA. The addition of ethanol also reduced the ciprofloxacin removal efficiency to 28.9%. Moreover, *t*-BuOH and BQ were used as the capture agents for hydroxyl radicals ($^{\bullet}OH$) and superoxide radicals ($^{\bullet}O_2^-$), respectively. As presented in Fig. 7d, only a loss of 5.4% was found for the ciprofloxacin degradation efficiency in the presence of the BQ scavenger, while the ciprofloxacin removal efficiency decreased from 76.8% to 23.8% with the *t*-BuOH scavenger. These results demonstrated that the existence of hydroxyl radicals, as well as holes in the system, were of great significance in the photocatalytic degradation of ciprofloxacin. However, superoxide radicals contributed the least for the ciprofloxacin degradation, which was in good agreement with the previous studies,[34] such as the photodegradation of ciprofloxacin over the magnetic 3D γ-Fe_2O_3@ZnO core–shell catalyst and the heterogeneous Fenton degradation of three kinds of antibiotics using the magnetic core–shell $MnFe_2O_4$@C-NH_2 catalyst.[35]

The reusability of the photocatalyst is significant to evaluate the potential of its practical application. Therefore, five

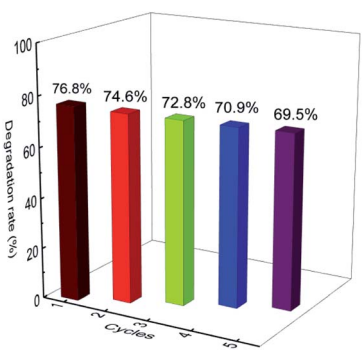

Fig. 8 Recycled experiments of the E-$Bi_2O_2CO_3$ photocatalyst.

consecutive cycles were performed, and the results are presented in Fig. 8. At the end of each experiment, the solid photocatalyst was filtered, washed with 50% ethanol water, and then dried in an oven at 60 °C overnight. The photocatalysis experiment was repeated with a ciprofloxacin concentration of 10 mg L^{-1} in the presence of the recycled catalyst at pH 7.12. It can be observed that the E-$Bi_2O_2CO_3$ photocatalyst maintained a high photocatalytic activity even after the fifth cycle. No distinct deactivation was observed since there was only 7.3% loss of the ciprofloxacin degradation rate after the last cycling. A slight loss of the used catalyst was inevitable during the recovery process, which might be one of the reasons for the reduction of the photocatalysis activity. These results indicated that the E-$Bi_2O_2CO_3$ photocatalyst possessed good stability and reusability.

4. Conclusions

Few-layer $Bi_2O_2CO_3$ nanosheets (E-$Bi_2O_2CO_3$) were successfully fabricated by a novel electrochemically cathodic exfoliation, followed by exposure to ambient condition. Compared to the $Bi_2O_2CO_3$ nanoparticles synthesized by hydrothermal method (H-$Bi_2O_2CO_3$), E-$Bi_2O_2CO_3$ showed superior activity in the photocatalytic degradation of ciprofloxacin antibiotic under UV-Vis light irradiation. The enhanced catalytic performance of E-$Bi_2O_2CO_3$ was due to the ultrathin structure, which enlarged the specific surface area and reduced the band gap. The trapping experiments confirmed that the holes, as well as hydroxyl radicals, were the major contributors for the ciprofloxacin degradation, while the superoxide radicals showed negligible contribution for ciprofloxacin decomposition. Finally, E-$Bi_2O_2CO_3$ showed good reusability and had a bright application prospect in the treatment of antibiotic wastewater.

Conflicts of interest

There are no conflicts to declare.

Acknowledgements

The authors would like to convey their gratitude for the financial support from the National Natural Science Foundation of China (21805211, 51862033), Department of Education of Guizhou Province (QJHKYZ[2020]042, KY[2016]009), and the Science and Technology Foundation of Guizhou Province (JC[2017]1185, JC[2018]1164, ZC[2020]2Y037, PTRC[2017]5604, QKHJC-ZK[2021]YB071).

Notes and references

1 L. Wang, J. Yang, Y. Li, J. Lv and J. Zou, *Chem. Eng. J.*, 2016, **284**, 1058–1067.
2 N. S. Shah, J. Ali Khan, M. Sayed, Z. Ul Haq Khan, H. Sajid Ali, B. Murtaza, H. M. Khan, M. Imran and N. Muhammad, *Chem. Eng. J.*, 2019, **356**, 199–209.
3 A. S. Giri and A. K. Golder, *J. Environ. Sci.*, 2019, **80**, 82–92.
4 S. Sood, S. K. Mehta, A. S. K. Sinha and S. K. Kansal, *Chem. Eng. J.*, 2016, **290**, 45–52.
5 Y. Zhao, X. Liang, Y. Wang, H. Shi, E. Liu, J. Fan and X. Hu, *J. Colloid Interface Sci.*, 2018, **523**, 7–17.
6 S. K. Kansal, S. Sood, A. Umar and S. K. Mehta, *J. Alloys Compd.*, 2013, **581**, 392–397.
7 A. H. Ali, S. Kapoor and S. K. Kansal, *Desalin. Water Treat.*, 2011, **25**, 268–275.
8 H. Cheng, B. Huang, P. Wang, Z. Wang, Z. Lou, J. Wang, X. Qin, X. Zhang and Y. Dai, *Chem. Commun.*, 2011, **47**, 7054–7056.
9 Y. Liu, Z. Wang, B. Huang, X. Zhang, X. Qin and Y. Dai, *J. Colloid Interface Sci.*, 2010, **348**, 211–215.
10 T. Zhao, J. Zai, M. Xu, Q. Zou, Y. Su, K. Wang and X. Qian, *CrystEngComm*, 2011, **13**, 4010–4017.
11 Y. Liu, Z. Wang, B. Huang, K. Yang, X. Zhang, X. Qin and Y. Dai, *Appl. Surf. Sci.*, 2010, **257**, 172–175.
12 Y. Ao, L. Xu, P. Wang, C. Wang, J. Hou, J. Qian and Y. Li, *Appl. Surf. Sci.*, 2015, **355**, 411–418.
13 C. Yang, G. Gao, Z. Guo, L. Song, J. Chi and S. Gan, *Appl. Surf. Sci.*, 2017, **400**, 365–374.
14 G. Cheng, H. Yang, K. Rong, Z. Lu, X. Yu and R. Chen, *J. Solid State Chem.*, 2010, **183**, 1878–1883.
15 S. Peng, L. Li, H. Tan, Y. Wu, R. Cai, H. Yu, X. Huang, P. Zhu, S. Ramakrishna, M. Srinivasan and Q. Yan, *J. Mater. Chem. A*, 2013, **1**, 7630–7638.
16 Y. Zhang, X. Zhang, Y. Ling, F. Li, A. M. Bond and J. Zhang, *Angew. Chem., Int. Ed.*, 2018, **57**, 13283–13287.
17 M. Chen, J. Yao, Y. Huang, H. Gong and W. Chu, *Chem. Eng. J.*, 2018, **334**, 453–461.
18 M. Pumera and Z. Sofer, *Adv. Mater.*, 2017, **29**, 1605299.
19 S. Yang, K. Zhang, A. G. Ricciardulli, P. Zhang, Z. Liao, M. R. Lohe, E. Zschech, P. W. Blom, W. Pisula and K. Müllen, *Angew. Chem.*, 2018, **130**, 4767–4771.
20 F. Yang, F. Yu, Z. Zhang, K. Zhang, Y. Lai and J. Li, *Chem.–Eur. J.*, 2016, **22**, 2333–2338.
21 Z. Lin, Y. Liu, U. Halim, M. Ding, Y. Liu, Y. Wang, C. Jia, P. Chen, X. Duan, C. Wang, F. Song, M. Li, C. Wan, Y. Huang and X. Duan, *Nature*, 2018, **562**, 254–258.
22 W. Hong, A. Wang, L. Li, T. Qiu, J. Li, Y. Jiang, G. Zou, H. Peng, H. Hou and X. Ji, *Adv. Funct. Mater.*, 2020, 2000756.
23 H. Qin, R. Xiao, W. Shi, Y. Wang, H. Li, L. Guo, H. Cheng and J. Chen, *RSC Adv.*, 2018, **8**, 33972–33979.
24 R. Wang, X. Li, W. Cui, Y. Zhang and F. Dong, *New J. Chem.*, 2015, **39**, 8446–8453.
25 J. Zhang, J. Yu, Y. Zhang, Q. Li and J. R. Gong, *Nano Lett.*, 2011, **11**, 4774–4779.
26 Y. Zheng, F. Duan, M. Chen and Y. Xie, *J. Mol. Catal. A: Chem.*, 2010, **317**, 34–40.
27 F. Dong, J. Bian, Y. Sun, T. Xiong and W. Zhang, *CrystEngComm*, 2014, **16**, 3592–3604.
28 F. Dong, Y. Sun, M. Fu, W.-K. Ho, S. C. Lee and Z. Wu, *Langmuir*, 2012, **28**, 766–773.
29 Y. Wang, H. Zhao, M. Li, J. Fan and G. Zhao, *Appl. Catal., B*, 2014, **147**, 534–545.
30 S. Sood, A. Umar, S. Kumar Mehta and S. Kumar Kansal, *Ceram. Int.*, 2015, **41**, 3355–3364.

31 J. Hou, C. Yang, Z. Wang, S. Jiao and H. Zhu, *Appl. Catal., B*, 2013, **129**, 333–341.
32 W. Li, D. Li, Y. Lin, P. Wang, W. Chen, X. Fu and Y. Shao, *J. Phys. Chem. C*, 2012, **116**, 3552–3560.
33 R. Palominos, J. Freer, M. A. Mondaca and H. D. Mansilla, *J. Photochem. Photobiol., A*, 2008, **193**, 139–145.
34 N. Li, J. Zhang, Y. Tian, J. Zhao, J. Zhang and W. Zuo, *Chem. Eng. J.*, 2017, **308**, 377–385.
35 H. Qin, H. Cheng, H. Li and Y. Wang, *Chem. Eng. J.*, 2020, **396**, 125304.